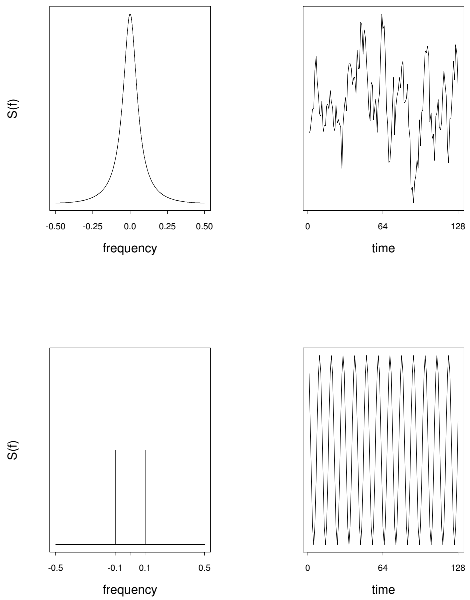

Figure 18: Top row: example of a purely continuous spectrum (left) and one realization of length 128 (right).
Bottom row: example of a purely discrete spectrum (left) and one realization of length 128 (right).

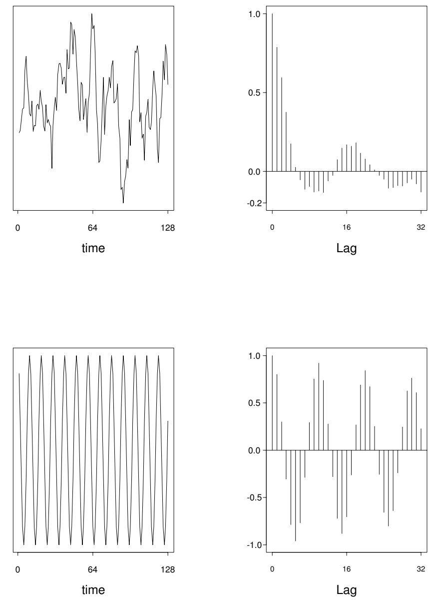

Figure 19: Top row: realization of process with purely continuous spectrum (left) and sample autocorrelation (right).
Bottom row: realization of process with purely discrete spectrum (left) and sample autocorrelation (right).

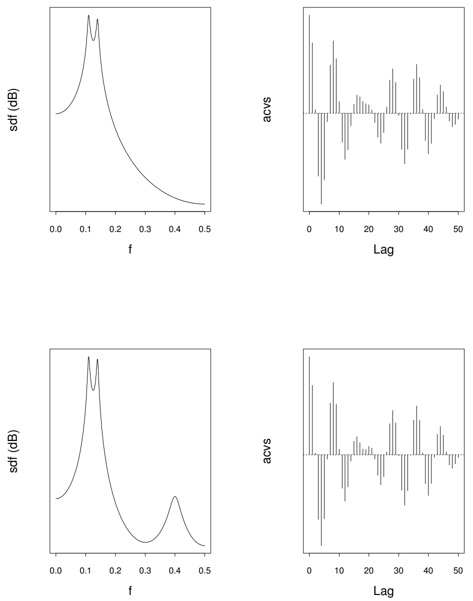

Figure 20: Two spectral density functions (left) and their corresponding autocovariance sequences (right).

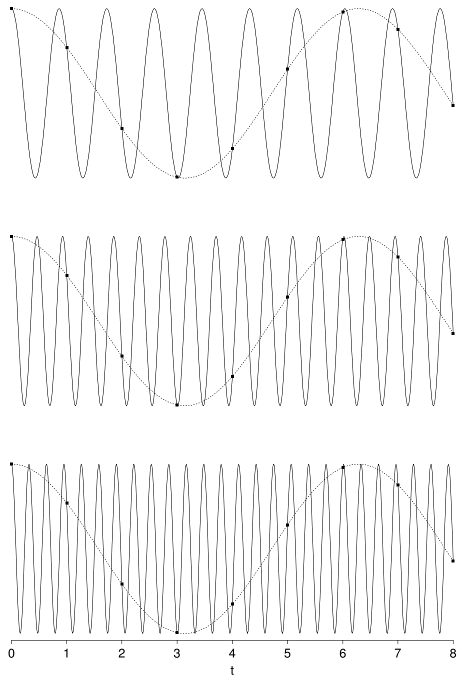

Figure 21: Illustration of the aliasing effect. The dotted curves above show $\cos(t)$ versus t. The solid curves show $\cos([1 + 2k\pi]t)$ versus t for (from top to bottom) $k = 1, 2$ and 3. The solid black squares show the common value of all four sinusoids when sampled at $t = 0, 1, \ldots, 8$.

Fig 21a: The concept of aliasing illustrated for two different sample intervals. In each picture the thin black line is the continuous spectrum, and the thick black line is the resulting spectrum for the discrete process (which is periodic, as shown by its continuation with the thick grey line).

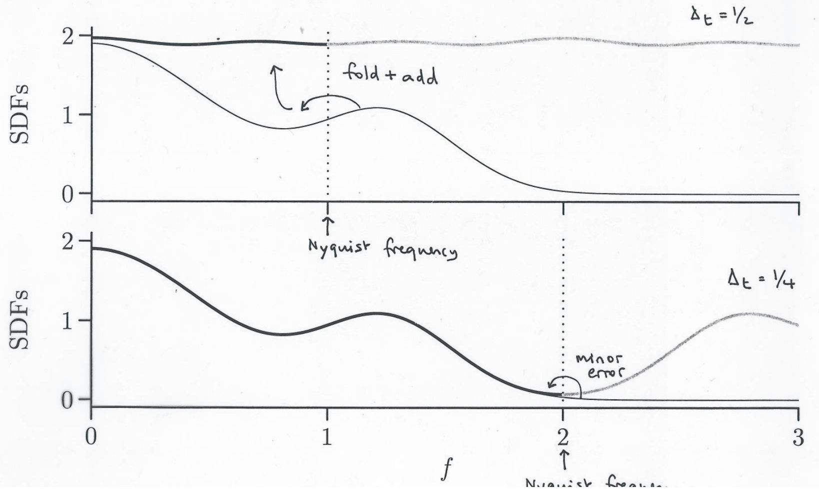

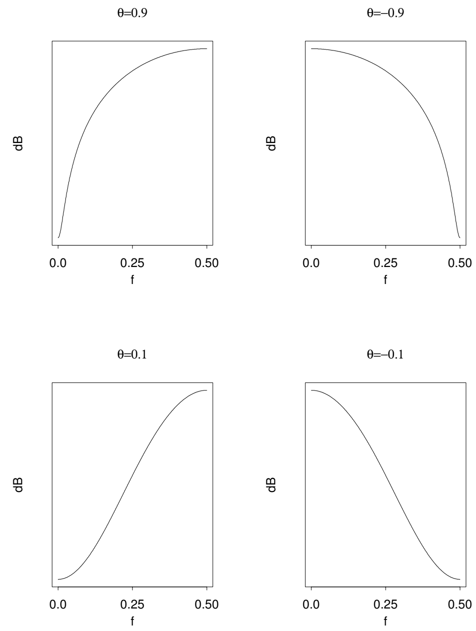

Figure 22: Examples of MA(1) spectra – when $\theta_{1,1}$ is positive we have a high frequency spectrum and when $\theta_{1,1}$ is negative we have a low frequency spectrum

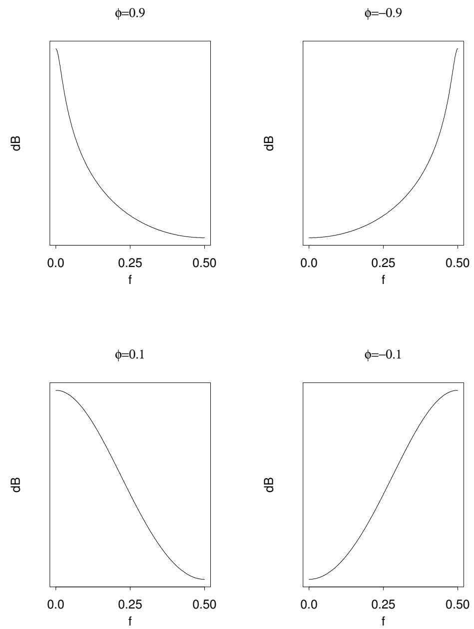

Figure 23: Examples of AR(1) spectra – when $\phi_{1,1}$ is positive we have a low frequency spectrum and when $\phi_{1,1}$ is negative we have a high frequency spectrum

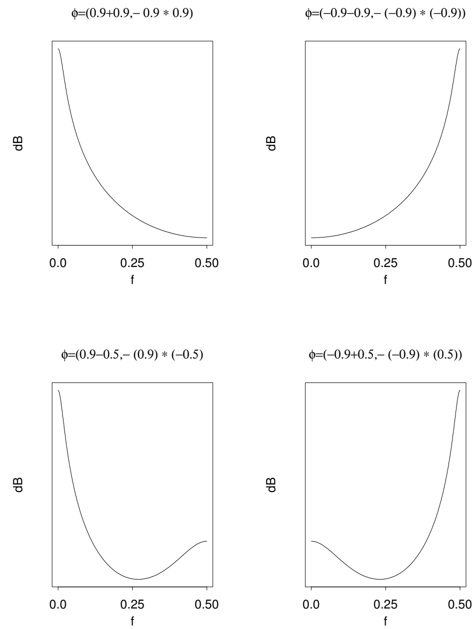

Figure 24: Examples of AR(2) spectra with real characteristic reciprocal roots, $a = r_1$ and $b = r_2$, giving AR parameter values of: $\phi_{1,2} = r_1 + r_2$ and $\phi_{2,2} = -r_1 r_2$

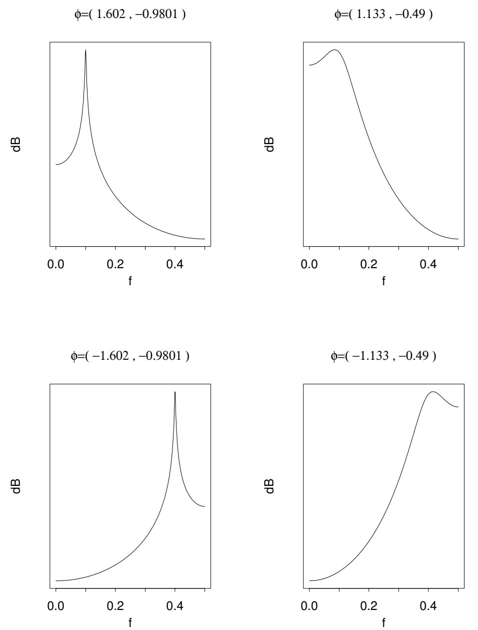

Figure 25: Examples of AR(2) spectra with complex characteristic reciprocal roots, $re^{\pm i2\pi f}$, with $r = 0.99$ for the plots in the left column and $r = 0.7$ for the plots in the right column, and $f = 0.1$ for the plots in the first row, and $f = 0.4$ for the plots in the second row, the AR parameter values (as shown in the titles) can be calculated from $\phi_{1,2} = 2r\cos(2\pi f)$ and $\phi_{2,2} = -r^2$

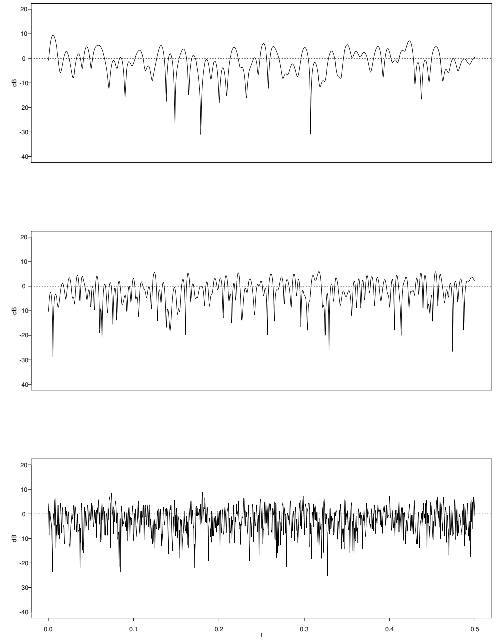

Figure 26: Inconsistency of the periodogram. The plots show the periodogram (on a decibel scale) of a unit variance white noise process of length (from top to bottom) $N = 128, 256$ and 1024. The horizontal dashed line indicates the true sdf.

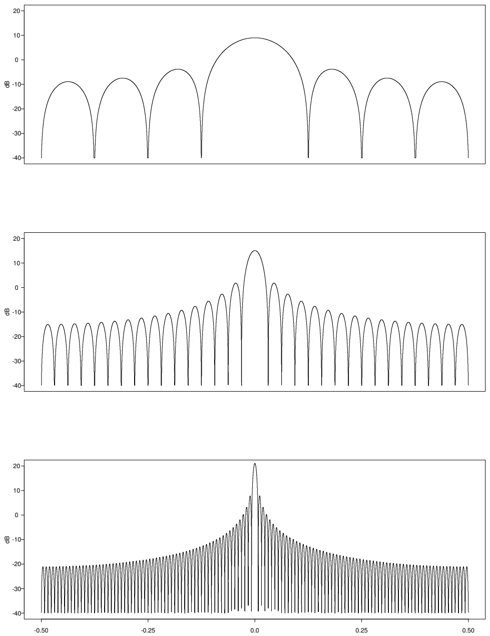

Figure 27: Fejér's kernel for sample sizes $N = 8, 32$ and 128

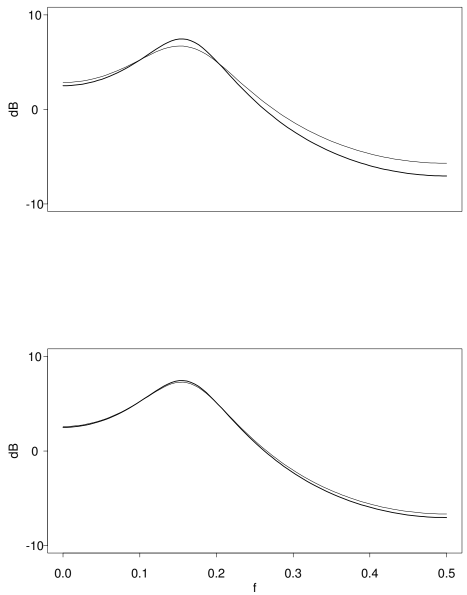

Figure 28: Bias properties of the periodogram for an AR(2) process with low dynamic range. The thick curves are the true sdf $S(f)$, while the thin curves are $\mathrm{E}\{\hat{S}^{(p)}(f)\}$ for sample sizes (from top to bottom) $N = 16$ and 64.

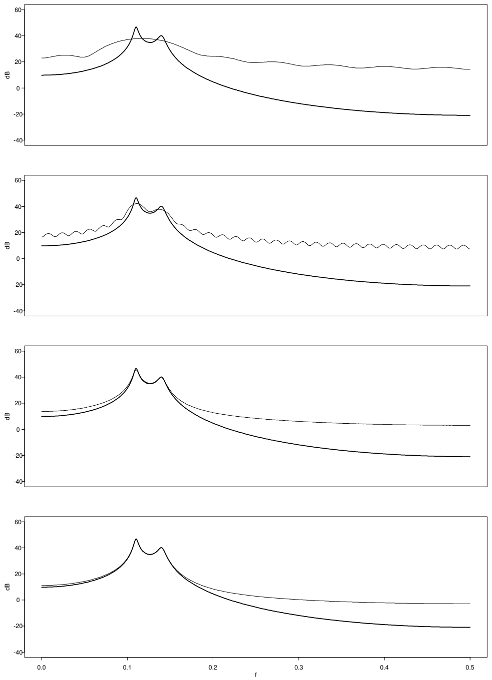

Figure 29: Bias properties of the periodogram for an AR(4) process with high dynamic range. The thick curves are the true sdf $S(f)$, while the thin curves are $\mathrm{E}\{\hat{S}^{(p)}(f)\}$ for sample sizes (from top to bottom) $N = 16, 64, 256$ and 1024.

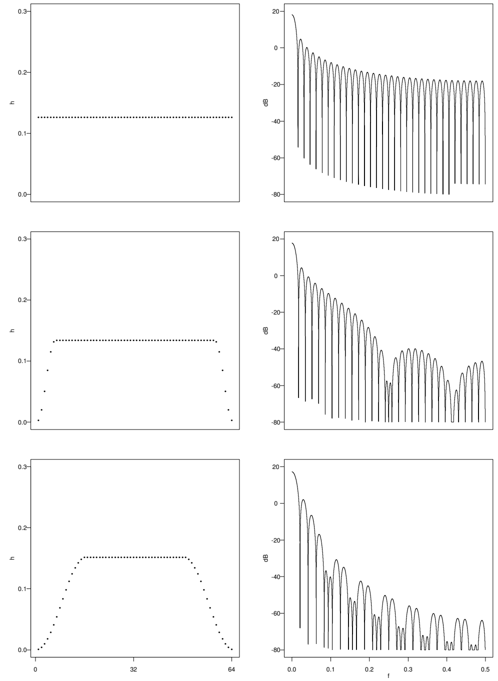

Figure 30: Different data tapers (left column) and associated spectral windows $\mathcal{H}(f)$ (right column), for $N = 64$.

The tapers are a rectangular taper (top), a 20% (middle) and 50% (bottom) split cosine bell taper.

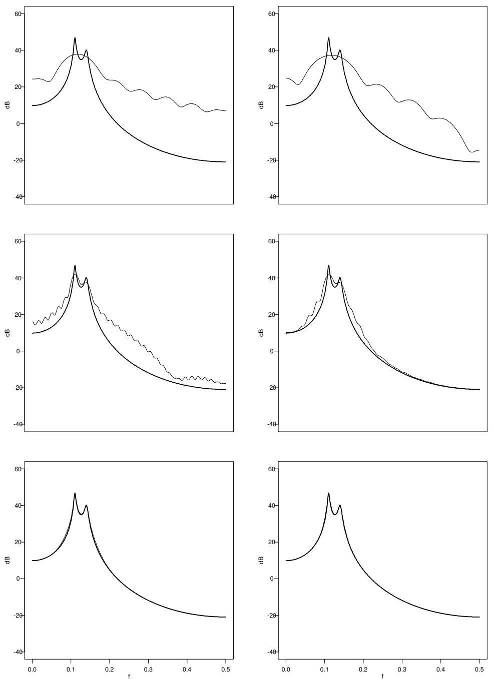

Figure 31: Bias properties of direct spectral estimators for an AR(4) process with high dynamic range, using a 20% (left column) and 50% (right column) split cosine bell taper. The thick curves are the true sdf $S(f)$, while the thin curves are $\mathrm{E}\{\hat{S}^{(p)}(f)\}$ for sample sizes (from top to bottom) $N = 16, 64$ and 256.

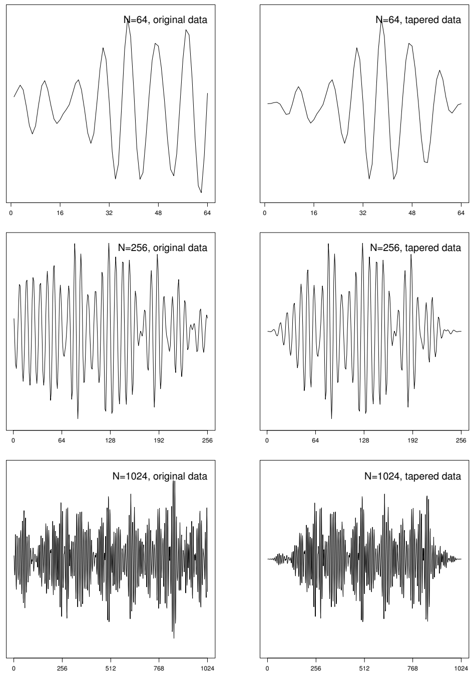

Figure 32: The left column shows simulations from the AR(4) model:
$X_t = 2.7607X_{t-1} - 3.8106X_{t-2} + 2.6535X_{t-3} - 0.9258X_{t-4} + \epsilon_t$
For (from top to bottom) $N = 64, 256$ and 1024.
The right column shows $\{X_t h_t\}$ where $\{h_t\}$ is the appropriate length 50% split cosine bell taper.

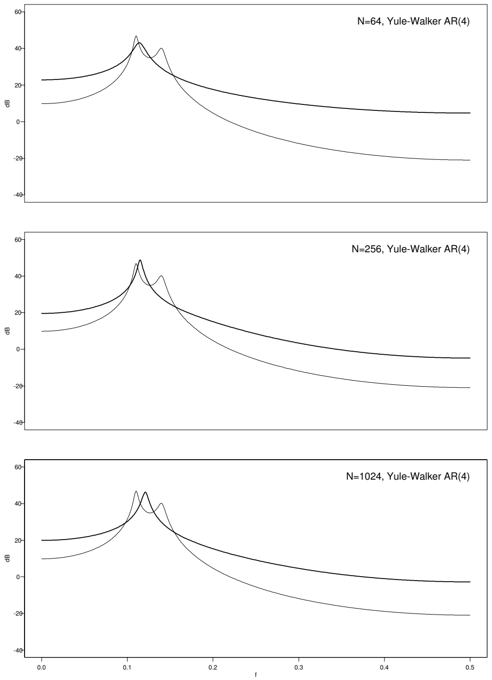

Figure 33: The thick line shows the spectrum of the AR(4) process associated with the Yule-Walker estimates of $\phi_{1,4}, \ldots, \phi_{4,4}$, for the sequences shown in the left column of Figure 32 (i.e. untapered). The thin line shows the true spectrum.

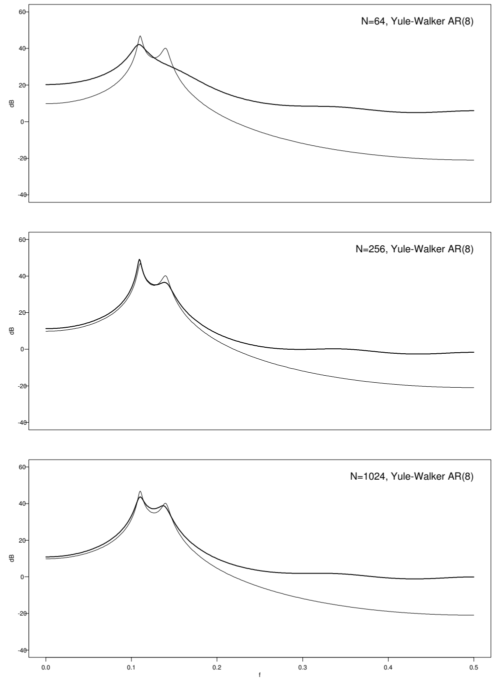

Figure 34: The thick line shows the spectrum of the AR(8) process associated with the Yule-Walker estimates of $\phi_{1,8}, \ldots, \phi_{8,8}$, for the sequences shown in the left column of Figure 32 (i.e. untapered). The thin line shows the true spectrum.

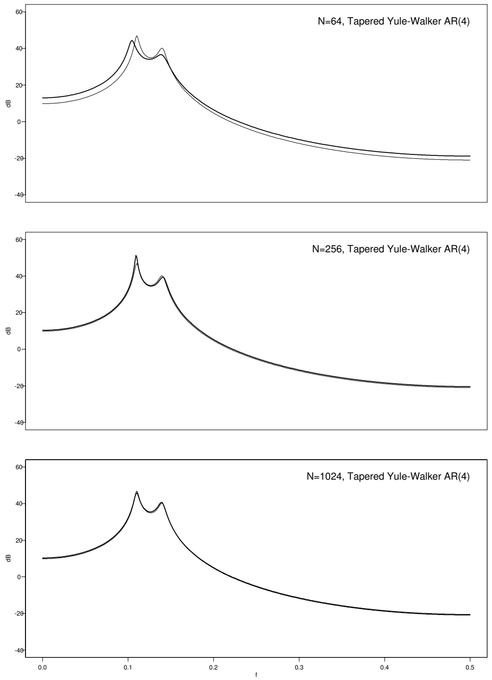

Figure 35: The thick line shows the spectrum of the AR(4) process associated with the Yule-Walker estimates of $\phi_{1,4}, \ldots, \phi_{4,4}$, for the sequences shown in the right column of Figure 32 (i.e. tapered). The thin line shows the true spectrum.